Hall, J. S. and Michaels, J.E., "Minimum variance ultrasonic imaging applied to an *in situ* sparse guided wave array," *IEEE Trans. Ultrason. Ferroelectr. Freq. Control*, **57** (10), pp. 2311-2323, 2010

# Minimum Variance Ultrasonic Imaging Applied to an *in situ* Sparse Guided Wave Array

James S. Hall, *Student Member, IEEE*, and Jennifer E. Michaels, *Senior Member, IEEE*

***Abstract*—Ultrasonic guided wave imaging with a sparse, or spatially distributed, array can detect and localize damage over large areas. Conventional delay-and-sum images from such an array typically have a relatively high noise floor, however, and contain artifacts that often cannot be discriminated from damage. Considered here is minimum variance distortionless response (MVDR) imaging, which is a variation of delay-and-sum imaging, whereby weighting coefficients are adaptively computed at each pixel location. Utilization of MVDR significantly improves image quality compared to delay-and-sum imaging, and additional improvements are obtained from incorporation of *a priori* scattering information in the MVDR method, use of phase information, and instantaneous windowing. Simulated data from a through-hole scatterer are used to illustrate performance improvements, and a performance metric is proposed that allows for quantitative comparisons of images from a known scatterer. Experimental results from a through-hole scatterer are also provided that illustrate imaging efficacy.**

***Index Terms*—ultrasonics, Lamb waves, sparse array, nondestructive evaluation, structural health monitoring, imaging, beamforming, sidelobe reduction, artifact reduction, minimum variance, Capon's method, phase information**

## I. Introduction

Guided waves play a key role in proposed and existing methods for structural health monitoring (SHM) and nondestructive evaluation (NDE). They allow large plate-like structures, such as aircraft skins, ship hulls, and large storage tank walls, to be interrogated for surface and subsurface defects since the waves are able to propagate over long distances with reduced geometric losses compared to bulk wave propagation [1]. However, the long distances traveled complicate damage detection and localization efforts because the received ultrasonic signals invariably contain multiple overlapping reflections from boundaries and internal geometric reflectors. These overlapping reflections appear in images generated from guided waves as artifacts that are often indistinguishable from actual damage. This paper builds upon previous work by the authors [2, 3], in which the use of Minimum Variance Distortionless Response (MVDR) [4] beamforming, also known as Capon's Method [5], is employed to minimize these artifacts. In addition, scattering fields, phase information, and time-domain windowing are used in conjunction with MVDR to further improve image quality. This work is presented in the context of Lamb wave propagation between spatially distributed array elements, where the interrogation area is located in the near-field of the array aperture, although it is also applicable to compact array geometries for both bulk and guided waves. As such, this paper compliments that by Velichko and Wilcox [6], which focuses on imaging with compact linear and circular arrays under far-field plane wave assumptions.

This work was supported by NASA's Graduate Student Research Program, Grant No. NNX08AY93H, and the Air Force Office of Scientific Research, Grant No. FA9550-08-1-0241.

Both authors are with the School of Electrical and Computer Engineering at the Georgia Institute of Technology, 777 Atlantic Dr., NW, Atlanta, GA 30332-0250 USA (phone: 404-894-2994; fax: 404-894-4641; e-mail: jennifer.michaels@ece.gatech.edu).

The paper is organized as follows: Section II provides a brief background on guided wave imaging. Section III reviews conventional delay-and-sum imaging and proposes an imaging performance metric. Section IV introduces MVDR imaging and discusses additional techniques for image improvement. Section V discusses MVDR imaging in the context of NDE and SHM system concerns. Section VI presents experimental results, and Section VII contains the concluding remarks.

## II. Background

One underlying assumption common to all imaging techniques is that damage perturbs incident waves. To take advantage of changes in received signals resulting from the damage, guided wave imaging algorithms often use differenced information, meaning that baseline signals recorded prior to the introduction of any damage are subtracted from the current, or in-service, signals. The simple task of baseline subtraction has a number of challenges associated with it. Environmental changes can cause the received signals to change, even without the presence of damage. Wilcox *et al.* [7, 8] quantified the impact of baseline mismatch due to temperature changes and related this to a system's sensitivity to damage. Lu and Michaels [9] and Konstantinidis *et al.* [10] both addressed the problem of baseline subtraction by recording multiple baseline signals and using the baseline that resulted in the smallest residual; this signal is often referred to as the optimal baseline. Lu and Michaels [9] built upon this idea of optimal baseline subtraction by applying a stretch algorithm to the optimal baseline, further reducing residual signals. More recent work has further demonstrated compensation for near-homogeneous temperature changes [11-13]. Guided wave tomography, first suggested by Jansen [14] in 1990, is one of the earliest guided wave imaging techniques. Tomographic systems typically rely on either time-of-flight or amplitude information to generate an image located within a polygon bounding the ultrasonic transducers. A review of ultrasonic guided wave tomography is provided by Hay *et al.* [15]. More recently, Gao *et al.* [16] have proposed a tomographic-like algorithm that spatially distributes changes in guided wave signals between various transducer pairs. One of the limitations of these tomographic techniques is that a relatively large number of transducers around the perimeter of the imaging area is required to obtain a useful image. For commercial viability, it is desirable to minimize the number of transducers required to produce images for damage localization.

Sparse (i.e., spatially distributed) arrays of ultrasonic transducers have been proposed as a cost-effective means of integrating guided wave-based SHM and NDE methods into commercial and industrial applications. In 2004, Wang *et al.* [17] introduced a method for guided wave imaging that is applicable to sparse arrays. The technique was presented in the context of synthetic time-reversal but is typically referred to either as delay-and-sum imaging or the ellipse method. In this approach, each pixel value is based on the summation of the received signals at different points in time. The specific times are a function of the total distance from transmitter, to pixel location, to receiver. The ellipse nomenclature is derived from the fact that the locus of a constant time curve is an ellipse. Note that Wang *et al.* formulated the summation with weighting coefficients, but used uniform weights and did not discuss other choices of weighting coefficients. Michaels and Michaels [18] expanded the approach of Wang *et al*. to sum the signals over a time window of data, as opposed to a single point in time, establishing the pixel value as the energy contained within the resulting summed signal. Michaels *et al.* [19] later demonstrated improved imaging performance by applying an exponential window to each received signal beginning at the time of the direct arrival. Finally, Michaels and Michaels [20] showed that images generated from different frequency excitation signals could be fused to obtain higher-quality images.

Another technique has recently been introduced, the hyperbola algorithm [19, 21], which applies the delay-and-sum approach to cross-correlations between baseline subtracted signals. The hyperbola nomenclature is used because the locus of constant time differences between the same arrival at two receivers is a hyperbola. Because this method groups receivers in pairs with a third transmitting transducer to obtain cross-correlation information, there is a much larger number of contributing signals for imaging as compared to the ellipse algorithm. Although some of the techniques discussed here may be applicable to imaging with the hyperbola algorithm, the scope of this paper is focused on ellipse techniques using multiple transmit-receive pairs.

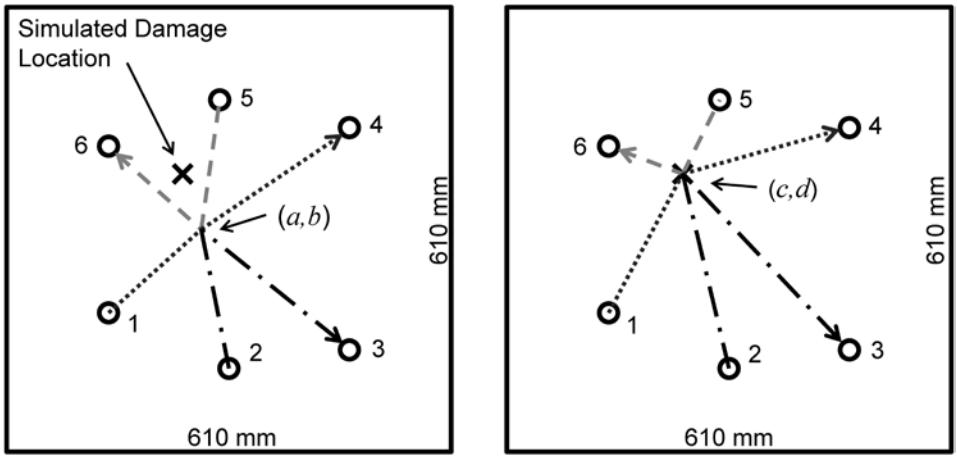


FIGURE 1. Diagram showing the plate dimensions and transducer arrangement for simulations and experiments. Location (*a*,*b*) is an imaging location away from the simulated damage, and (*c*,*d*) is the location of the simulated damage.

One additional challenge associated with guided wave imaging is geometric dispersion, meaning that the propagation speed of Lamb waves is frequency-dependent [22]. As such, signals spread in time as they propagate and thus decrease in amplitude [23]. The spreading of the signals is also accompanied by a change in phase. The phase change adversely impacts both the ellipse and hyperbola algorithms, which inherently assume that the scattered signals received at each transducer are in-phase. One common solution is to use the envelope of the differenced signals [24], which is the absolute value of the analytic representation of the signal. Some of the costs and benefits of using envelope vs. RF signals were identified by Wilcox *et al.* [25]. Alternatively, the dispersive nature of the waves can be addressed by dispersion compensation directly in the frequency domain as demonstrated by Sicard *et al.* [26], or by converting the time-domain signals to the spatial domain, as performed by Wilcox [27, 28].

## III. Delay-and-Sum Imaging

Consider the case of a homogeneous, isotropic plate with $N$ identical transducers, such as in Fig. 1 where $N = 6$. Although six transducers allow for $N(N-1) = 30$ different combinations, only one signal from each unique transmitter-receiver pair needs to be used, resulting in 15 signals. The two diagrams in Fig. 1 show the propagation paths for three of the 15 transmitter-receiver pairs. Figure 1(a) depicts the paths for location (*a*,*b*) and Figure 1(b) depicts the corresponding paths for location (*c*,*d*). It is assumed that perfect baseline subtraction is achieved, resulting in differenced signals comprising only the scattered field from the damage.

We first consider the case whereby the envelopes of the scattered signals are used for imaging. The envelope is obtained by taking the absolute value of the analytic representation of the scattered signal:

$$r_{ij}^{\mathrm{ENV}}(t) = \left| s_{ij}(t) + j\hat{s}_{ij}(t) \right|, \tag{1}$$

where $s_{ij}(t)$ is the RF scattered signal generated by transmitting from the $i$th transducer and receiving at the $j$th transducer, $\hat{s}_{ij}(t)$ is the Hilbert transform of the RF scattered field, $j$ is the square root of −1, and $r_{ij}^{\mathrm{ENV}}(t)$ is the envelope signal.

Combining the imaging concepts of Wang *et al.* [17] and Michaels and Michaels [18], pixel values for delay-and-sum imaging are defined as:

$$P_{x,y} = \int \left| \sum_{i=1}^{N-1} \sum_{j=i+1}^{N} e_{ijxy} r_{ij}\left( t + \frac{d_{ixy} + d_{jxy}}{c_{\mathrm{g}}} \right) \right|^2 w(t)\,\mathrm{d}t, \tag{2}$$

where $w(t)$ is a windowing function, $d_{ixy}$ is the distance from the $i$th transducer to the pixel location $(x,y)$, $c_{\mathrm{g}}$ is the group velocity, and $e_{ijxy}$ is a weighting coefficient specific to the pixel location and transmitter-receiver pair. The signals $r_{ij}$ could be either RF or envelope.

At this point, it is desirable to simplify the notation in Eq. (2). First, it is possible to replace the dual

summation with a single summation of $M$ terms by re-indexing each term as appropriate:

$$P_{x,y} = \int \left| \sum_{m=1}^{M} e_{mxy} r_m \left( t + \frac{d_{mxy}}{c_g} \right) \right|^2 w(t)\,\mathrm{d}t. \quad (3)$$

The summation can be described in vector format as a function of the weighting coefficients:

$$P_{x,y}\left(\vec{\mathbf{e}}\right) = \int \left| \vec{\mathbf{r}}_{x,y}^{\mathrm{T}}(t)\vec{\mathbf{e}} \right|^2 w(t)\,\mathrm{d}t, \quad (4)$$

where the superscript "T" indicates the transpose. The first term in the right-hand-side of Eq. (4) contains the back-propagated signals, $\vec{\mathbf{r}}_{x,y}(t)$, organized as row vectors:

$$\vec{\mathbf{r}}_{x,y}(t) = \left[ r_1\left( t + \frac{d_{1xy}}{c_g} \right) \quad \cdots \quad r_M\left( t + \frac{d_{Mxy}}{c_g} \right) \right]^{\mathrm{T}}. \quad (5)$$

The second term, $\vec{\mathbf{e}}$, is a column vector containing the weighting coefficients. To facilitate discussion in the context of MVDR, $\vec{\mathbf{e}}$ is referred to as the "look direction." Throughout this paper, it is assumed that $\vec{\mathbf{e}}$ is normalized to have unit $L_2$ norm. After expanding the squared term of Eq. (4) into two complex conjugate terms, Eq. (4) can be simplified to:

$$P_{x,y}^{\mathrm{DS}}\left(\vec{\mathbf{e}}\right) = \vec{\mathbf{e}}^{\mathrm{H}} \mathbf{R}_{x,y} \vec{\mathbf{e}}. \quad (6)$$

In Eq. (6) the superscript "H" represents the Hermitian transpose, and the spatiotemporal correlation matrix, $\mathbf{R}_{x,y}$, is calculated over the time-window of interest:

$$\mathbf{R}_{x,y} = \int \vec{\mathbf{r}}_{x,y}^{*}(t)\vec{\mathbf{r}}_{x,y}^{\mathrm{T}}(t)\,w(t)\,\mathrm{d}t, \quad (7)$$

where the superscript "*" indicates the element-wise conjugation of a vector. From Eqs. (6) and (7), the pixel value, $P_{x,y}^{\mathrm{DS}}\left(\vec{\mathbf{e}}\right)$, is maximized when the back-propagated signal vectors, $\vec{\mathbf{r}}_{x,y}(t)$, are scalar multiples of the look direction, $\vec{\mathbf{e}}$, since their inner product will be maximized.

The envelopes of the received, differenced signals for the three transmitter-receiver pairs of Fig. 1 are shown in the top plot of Fig. 2. These signals were generated using a ray tracing model incorporating boundary reflections via the method of images, and were modeled without dispersion for demonstration purposes. The source time function was a 3-cycle, 250 kHz, Hanning windowed sinusoid. Scattering characteristics are based on through-hole scattering fields generated using the low frequency approximation derived by Grahn [29] for 250 kHz $S_0$ incident and scattered waves. Back-propagated signals for pixel locations (*a*,*b*) and (*c*,*d*), shown in the middle and bottom plots of Fig. 1, are clearly different. Back-propagated signals at the damage location, (*c*,*d*), all have similar appearance and are aligned in time, which is clearly not the case for the back-propagated signals at the non-damage location, (*a*,*b*). As a result, the pixel value for (*c*,*d*), when calculated as per Eq. (6), is expected to be higher than that for (*a*,*b*) or any other non-damage location. Note that the shaded regions correspond to the time window of interest.

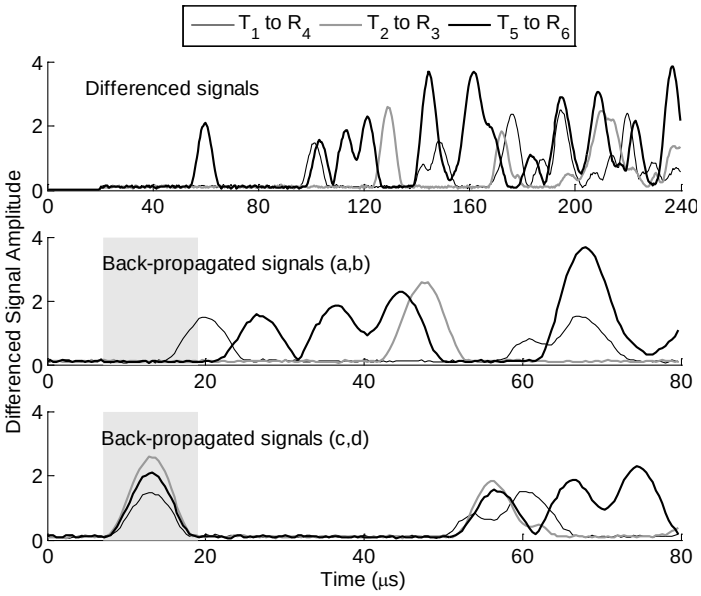


FIGURE 2. Received (top) and back-propagated (middle and bottom) signals. The shaded areas for the back-propagated signals indicate a 12 μs integration window centered at 13 μs.

Figure 3 shows the image generated using delay-and-sum imaging with a time window of 12 μs and with the weights inversely proportional to the square-root of the product of the propagation distances:

$$\vec{\mathbf{e}} \sim \left[ 1\Big/\sqrt{d_{1xy}^{\times}} \quad \cdots \quad 1\Big/\sqrt{d_{Mxy}^{\times}} \right]^{\mathrm{T}}, \quad (8)$$

where $d_{mxy}^{\times}$ is the product of the distances $d_{ixy}$ and $d_{jxy}$ defined in Eq. (2). The multiplication of propagation distances is necessary to accurately reflect the geometric spreading from both the source and the scatterer. Note that the weights are selected to maximize the pixel value at the damage location by matching the anticipated amplitude

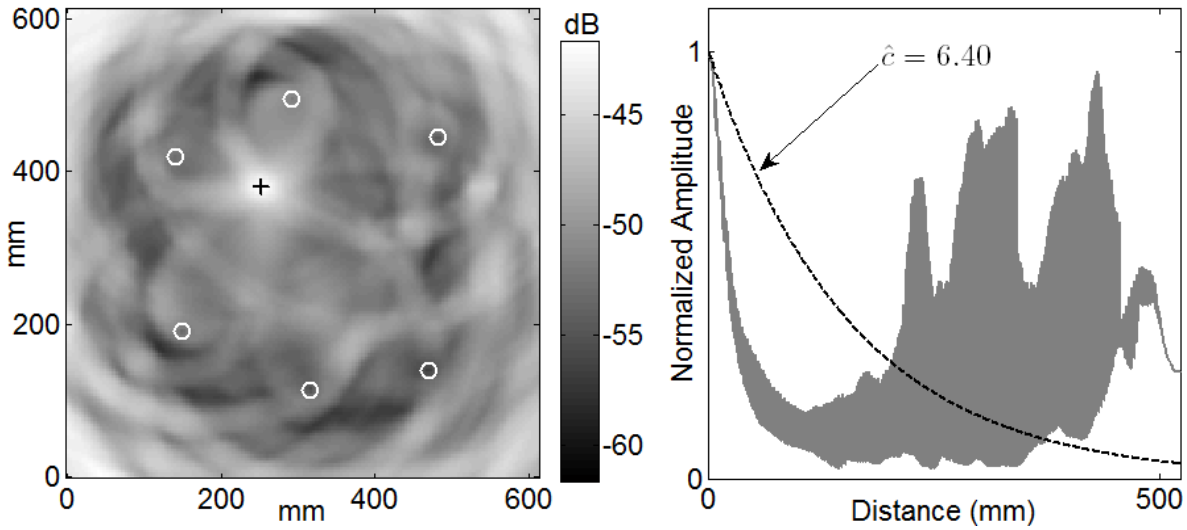


FIGURE 3. Delay-and-sum imaging using simulated envelope signals. (a) Image displayed using a 20 dB scale, and (b) normalized pixel values versus distance from damage location ( $\hat{c}$ = 6.40).

relationship between signals in the back-propagated signal vectors, $\bar{\mathbf{r}}_{x,y}(t)$.

In Fig. 3 and for the entirety of this paper, images are shown on a 20 dB scale, with the color scale aligned so that the peak value of the image corresponds to the top of the color bar. Figure 3(b) is a plot of the pixel values of Figure 3(a) as a function of distance from the simulated damage location. For the case when more than one pixel is located a specific distance from the true damage location, all of the pixel values are plotted, which results in a vertical distribution of points that extends from the smallest pixel value at that distance to the largest. The values are normalized so that the pixel value at the damage site is one. A perfect image would have a pixel value of one at a distance of zero and all other pixel values would be zero. Figure 3 illustrates that although the damage location can be identified, many artifacts are present that cannot be distinguished from damage on the basis of amplitude.

To effectively compare and contrast imaging methods, it is useful to establish a single quantitative measure of performance. Previously reported figures of merit, such as described in [20], do provide a means to evaluate images; however, it is desirable to characterize the quality of an image with a single scalar value.

A performance metric is proposed here that takes into account artifact amplitude, distance from damage, and overall noise floor. The proposed metric is the exponential coefficient, *c*, that results from a least-squares exponential curve fit to the pixel values, arranged as a function of distance from the damage location:

$$\frac{P(x)}{P(0)} \approx e^{-cx} \qquad \text{for } x \in X, \tag{9}$$

where $P(x)$ is the pixel value as a function of distance from the known damage location and $X$ is the set of all distances. This metric was chosen because it provides a single value that (1) increases (decreases) as the damage location becomes more focused (defocused), (2) increases (decreases) as the overall noise floor is lowered (raised), and (3) increases (decreases) as artifacts are moved towards (away from) the true damage site. In other words, the larger the value of *c*, the closer the image is to perfect (a single non-zero pixel value at the damage site), and artifacts are penalized more the further they are located from the true damage site. To find *c*, a least-squares fit is performed on the logarithmic values as:

$$\hat{c} = \arg\min_{c} \sum_{x \in X} \left( \ln\left(\frac{P(x)}{P(0)}\right) + cx \right)^2. \tag{10}$$

It is also important to note that this metric is only valid if the damage location is precisely known, such as for simulations and controlled experiments. Although this restriction limits widespread applicability, it still provides a mechanism for quantitatively comparing images and algorithms.

The exponential curve overlaid on Fig. 3(b) represents the curve that minimizes the performance metric of Eq. (10). For this image, $\hat{c}$ = 6.4.

## IV. MVDR IMAGING

Minimum Variance Distortionless Response (MVDR) imaging [4], also known as Capon's Method [5], is a covariance technique that can be used to improve imaging performance. In this section the mathematical basis for MVDR imaging is first reviewed and then various aspects of MVDR are considered that affect imaging efficacy.

### *A. Mathematical Basis of MVDR*

To begin, consider the following eigendecomposition of the correlation matrix in Eq. (7):

$$\mathbf{R}_{x,y} = \sum_{i=1}^{M} \lambda_i \vec{\mathbf{v}}_i \vec{\mathbf{v}}_i^{\mathrm{H}}, \tag{11}$$

where $\lambda_i$ are eigenvalues and $\vec{\mathbf{v}}_i$ are unit-norm eigenvectors specific to the correlation matrix $\mathbf{R}_{x,y}$. Since the correlation matrix is Hermetian symmetric, each eigenvalue is non-negative and the eigenvectors are orthogonal to one another. Throughout the paper, the eigenvalues are assumed to be ordered from largest to smallest, so $\vec{\mathbf{v}}_1$ will always be the eigenvector corresponding to $\lambda_1$, the largest eigenvalue.

Consider the set of backpropagated signals corresponding to a pixel location that exactly coincides with a scattering location, such as the back-propagated signals for (*c*,*d*) in Fig. 2. For an ideal scatterer and no additional echoes, each back-propagated signal comprises a common signal, *x*(*t*), that is zero outside of the window of interest and scaled according to some relationship, $\vec{\mathbf{s}}$, which is constrained to have unit-norm:

$$\vec{\mathbf{r}}_{c,d}(t) = x(t)\vec{\mathbf{s}}. \tag{12}$$

From the eigendecomposition of the correlation matrix for this simple case, the unit-norm relationship between signals, $\vec{\mathbf{s}}$, is equal to $\vec{\mathbf{v}}_1$, the energy of *x*(*t*) is equal to $\lambda_1$, and all other eigenvalues are zero:

$$\mathbf{R}_{c,d} = \int |x(t)|^2 w(t) \vec{\mathbf{s}} \vec{\mathbf{s}}^{\mathrm{H}} \mathrm{d}t = \lambda_1 \vec{\mathbf{v}}_1 \vec{\mathbf{v}}_1^{\mathrm{H}}. \tag{13}$$

By substituting Eq. (13) into Eq. (6), one can see that the pixel value $P_{c,d}^{\mathrm{DS}}(\vec{\mathbf{e}})$ is maximized at a value of $\lambda_1$ when $\vec{\mathbf{e}} = \vec{\mathbf{v}}_1 = \vec{\mathbf{s}}$ and minimized at a value of 0 when $\vec{\mathbf{e}} \perp \vec{\mathbf{v}}_1$. In other words, if the look direction, $\vec{\mathbf{e}}$, accurately reflects the amplitude relationship between signals, the pixel value is maximized.

To reduce image artifacts, it is desirable to minimize the pixel value for any location that does not correspond to damage. By assuming that the look direction, $\vec{\mathbf{e}}$, represents the amplitude relationship between signals in the case that damage is present at a pixel location, such as in Eq. (8), a constrained optimization problem can be constructed:

$$\min \overline{\mathbf{w}}^{\mathrm{H}} \mathbf{R}_{x,y} \overline{\mathbf{w}} \quad \text{such that} \quad \overline{\mathbf{w}}^{\mathrm{H}} \vec{\mathbf{e}} = 1. \tag{14}$$

Here $\overline{\mathbf{w}}$ represents a vector of optimal weights that satisfies Eq. (14). In words, the $\min \overline{\mathbf{w}}^{\mathrm{H}} \mathbf{R}_{x,y} \overline{\mathbf{w}}$ term minimizes the pixel value at all locations, while the constraint of the inner product of $\overline{\mathbf{w}}$ and $\vec{\mathbf{e}}$ preserves the pixel value at damage locations. The preservation of pixel values by the constraint can be made clear with a brief example. Recall that for the pixel value at (*c*,*d*) described in the previous section, the pixel value is maximized at a value of $\lambda_1$ when $\vec{\mathbf{e}} = \vec{\mathbf{s}} = \vec{\mathbf{v}}_1$. Substituting Eq. (13) into the left-hand-side of Eq. (14) and replacing $\vec{\mathbf{v}}_1$ with $\vec{\mathbf{e}}$ yields,

$$\overline{\mathbf{w}}^{H} \mathbf{R}_{c,d} \overline{\mathbf{w}} = \lambda_1 \left| \overline{\mathbf{w}}^{\mathrm{H}} \vec{\mathbf{e}} \right|^2. \tag{15}$$

Therefore, by constraining the inner product of $\overline{\mathbf{w}}$ and $\vec{\mathbf{e}}$ to have unit value, the pixel value at damage locations is preserved at a value of $\lambda_1$.

The optimal solution to this minimization problem can be found through the use of a Lagrange multiplier, $\alpha$, to satisfy the look direction constraint,

$$L = \overline{\mathbf{w}}^{\mathrm{H}} \mathbf{R}_{x,y} \overline{\mathbf{w}} + \alpha \left( \overline{\mathbf{w}}^{\mathrm{H}} \vec{\mathbf{e}} - 1 \right). \tag{16}$$

The Lagrangian *L* is minimized by taking the derivative of Eq. (16) with respect to $\overline{\mathbf{w}}$ and setting it equal to zero, which results in:

$$\overline{\mathbf{w}} = -\frac{\alpha}{2} \mathbf{R}_{x,y}^{-1} \vec{\mathbf{e}}. \tag{17}$$

By substituting the above equation for $\overline{\mathbf{w}}$ into the inner product constraint of Eq. (14), $\alpha$ can readily be shown to be:

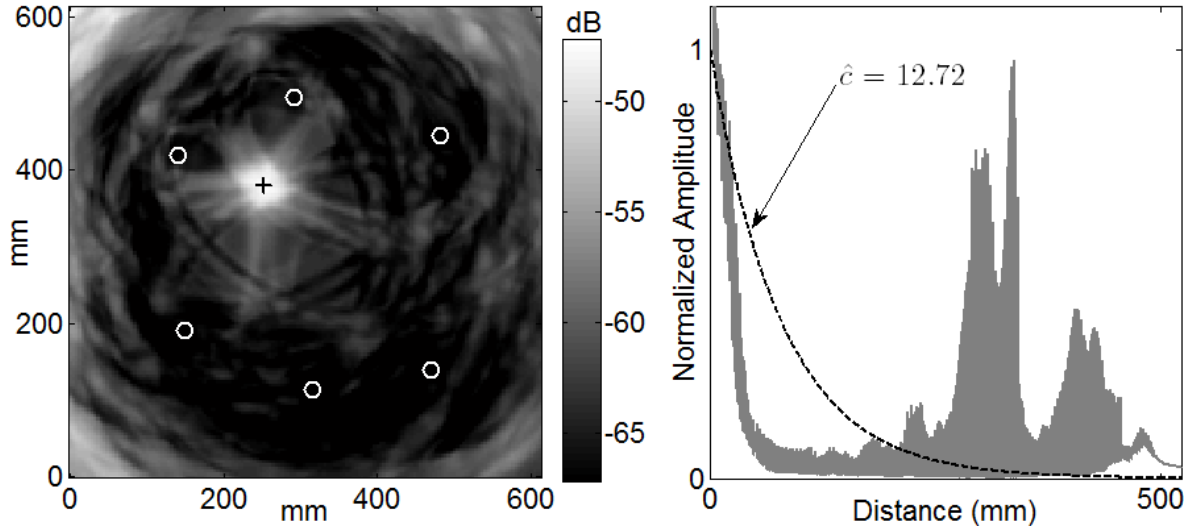


FIGURE 4. MVDR imaging using simulated envelope signals. (a) Image displayed using a 20 dB scale, and (b) normalized pixel values versus distance from damage location ( $\hat{c}$ = 12.72).

$$\alpha = -\frac{2}{\vec{\mathbf{e}}^{\mathrm{H}}\mathbf{R}_{x,y}^{-1}\vec{\mathbf{e}}}. \tag{18}$$

By further substituting the above equation for $\alpha$ back into Eq. (17), a closed-form expression for $\vec{\mathbf{w}}$ that satisfies Eq. (14) is obtained:

$$\vec{\mathbf{w}}\left(\vec{\mathbf{e}}\right) = \frac{\mathbf{R}_{x,y}^{-1}\vec{\mathbf{e}}}{\vec{\mathbf{e}}^{\mathrm{H}}\mathbf{R}_{x,y}^{-1}\vec{\mathbf{e}}}. \tag{19}$$

Using this equation, $\vec{\mathbf{w}}$ can be computed at each pixel location.

MVDR imaging is performed in a similar fashion to delay-and-sum imaging; however, instead of using the look direction directly, the optimal weights, $\vec{\mathbf{w}}\left(\vec{\mathbf{e}}\right)$, are calculated and used:

$$P_{x,y}^{\mathrm{MV}}\left(\vec{\mathbf{e}}\right) = \vec{\mathbf{w}}^{\mathrm{H}}\left(\vec{\mathbf{e}}\right)\mathbf{R}_{x,y}\vec{\mathbf{w}}\left(\vec{\mathbf{e}}\right), \tag{20}$$

where $\vec{\mathbf{w}}\left(\vec{\mathbf{e}}\right)$ is defined as in Eq. (19). Figure 4 shows imaging performance with MVDR using the same $\vec{\mathbf{e}}$ as given in Eq. (8). Visually, Fig. 4 clearly identifies the damage location with significantly reduced artifacts compared to Fig. 3. The performance metric $\hat{c}$ has increased from 6.4 to 12.7.

Note that the MVDR approach to imaging is an optimal solution to Eq. (14). As such, since Eq. (14) constrains the weights to reduce any energy that is not in the look direction, a reduction in artifact amplitudes should be expected over conventional delay-and-sum beamforming with the same look direction.

### *B. Modeling Errors and Regularization*

Although MVDR offers substantial improvement over conventional delay-and-sum imaging, careful consideration must be given to the operating environment and the implications of inaccurate modeling assumptions. Errors in transducer locations, transducer phase and gain differences, and inaccuracies inherent in the sampled approximation to the covariance matrix all constitute modeling errors that can severely degrade algorithmic performance if they are not accommodated.

As shown in [30], as signal-to-noise ratios increase, adaptive methods such as MVDR become increasingly sensitive to modeling errors. This sensitivity is in contrast to conventional imaging techniques that become less sensitive to modeling errors as signal-to-noise ratios increase. To address this problem, regularization of the matrix inverse in Eq. (19) is performed using diagonal loading [31], which is shown to be optimal for a number of constrained optimization problems [32], including Eq. (14) , and also addresses the scenario when an insufficient number of samples are used to generate the covariance matrix. The degree of diagonal loading can be described as some factor, *f*, of the largest eigenvalue, $\lambda_1$:

$$\mathbf{R}_{x,y}^{-1} = \left(\mathbf{R}_{x,y} + f\lambda_1\mathbf{I}\right)^{-1}. \tag{21}$$

Bounds can then be established for $f$, as described in [30]:

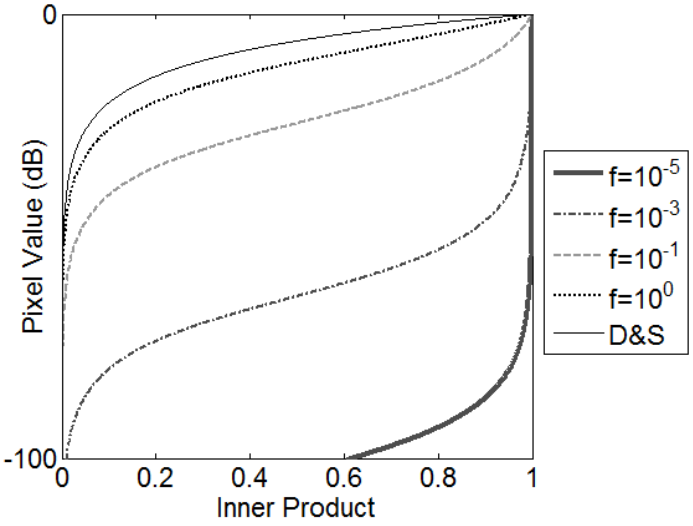


FIGURE 5. Pixel values as a function of inner product between look direction, $\vec{\mathbf{e}}$, and largest eigenvector, $\vec{\mathbf{v}}_1$. Four different regularization factors ($f$ = $10^{-5}$, $10^{-3}$, $10^{-1}$, $10^{0}$) are shown for MVDR imaging, which can be compared with the conventional delay-and-sum case (D&S).

$$\frac{1}{M} < \frac{\lambda_1}{f\lambda_1 + \sigma_n^2} < \frac{1}{\varepsilon}. \qquad (22)$$

Here $\sigma_n^2$ is the average noise power observed across all receivers and $\varepsilon$ is the degree of modeling error present in the unit look direction, $\vec{\mathbf{e}}$. The modeling error is quantified by the norm of the difference between the nominal look direction, $\vec{\mathbf{e}}$, and the "true" or "actual" look direction, $\hat{\mathbf{e}}$, which accurately reflects the underlying signal relationships within the received signals:

$$\varepsilon = \left\| \vec{\mathbf{e}} - \hat{\mathbf{e}} \right\|. \qquad (23)$$

Since the look direction is constrained to have unit norm, $\varepsilon$ will be in the range: $0 \le \varepsilon \le 2$. Rearranging Eq. (22) to solve for $f$ and assuming a large signal-to-noise ratio ( $\lambda_1 \gg \sigma_n^2$ ) reveals:

$$\varepsilon \le f < M. \qquad (24)$$

The lower bound for $f$ ensures that sufficient regularization is present to accommodate potential error in the look direction, while the upper bound prevents the regularization noise, $\lambda_1 f$, from unnecessarily degrading performance.

An example is provided here to illustrate the impact of regularization on MVDR performance. Consider a pixel location at which the cross-correlation matrix, $\mathbf{R}_{x,y}$, has a single, non-zero eigenvalue, $\lambda_1$, that is equal to one and $\vec{\mathbf{v}}_1$ is the ideal steering vector. Recall from Eq. (15) that the pixel value, $P_{x,y}^{MV}\left(\vec{\mathbf{e}}\right)$, is maximized at a value of $\lambda_1$ when $\vec{\mathbf{e}} = \vec{\mathbf{v}}_1$. Figure 5 illustrates the pixel value, $P_{x,y}^{MV}\left(\vec{\mathbf{e}}\right)$, as a function of the inner product between the look direction, $\vec{\mathbf{e}}$, and $\vec{\mathbf{v}}_1$ for several regularization values. As the regularization is increased, tolerance for inaccuracies in the look direction is also increased. This is apparent in Fig. 5 by comparing the pixel values that result when the inner product is close to, but not exactly, one. Unfortunately, the tolerance comes at the cost of larger artifacts, which can be seen by comparing the pixel values that result when $\vec{\mathbf{e}}$ and $\vec{\mathbf{v}}_1$ are not in agreement and produce an inner product much less than one. Therefore, to maximize the benefit of MVDR, it is desirable to use as little regularization as possible while keeping $f > \varepsilon$. To maintain consistency throughout the paper and allow for inaccuracies in the look direction when working with experimental data, a regularization factor of $10^{-1}$ is used for all MVDR imaging.

### *C. Scattering Characteristics*

With MVDR imaging, the look direction takes on a much more significant role than for delay-and-sum imaging. As such, further imaging improvements can be obtained by incorporating additional information into the look direction. Specifically, the look direction can be modified to incorporate information about the scatterer:

$$\vec{\mathbf{e}} \sim \left[ \psi_{x,y}^{1} \Big/ \sqrt{d_{1xy}^{\times}} \quad \cdots \quad \psi_{x,y}^{M} \Big/ \sqrt{d_{Mxy}^{\times}} \right]^{\mathrm{T}}, \qquad (25)$$

where $\psi_{x,y}^{k}$ corresponds to the scattering coefficient of an incident wave on point ($x$,$y$) for the $k$th transmitter-receiver pair. Note that as before, $\vec{\mathbf{e}}$ is scaled to be a unit-norm vector.

Significant effort has been expended by many researchers to accurately describe scattering fields for a number of defects. Surface-breaking defects of various sizes [33], through-thickness holes [34, 35], holes with and without symmetrical notches [36], and asymmetric scatterers such as notches [37] have been evaluated. As mentioned earlier, all through-hole scattering fields for this paper were generated using the low frequency

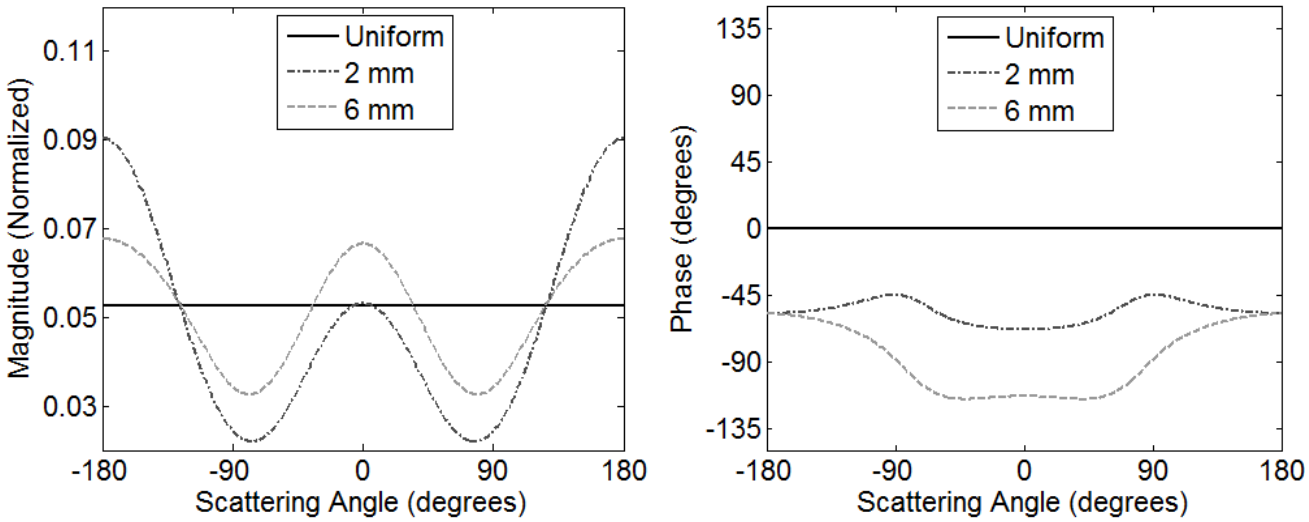


FIGURE 6. Scattering fields for a uniform scatterer compared to 2 mm and 6 mm through-holes generated as per Grahn [37]. The scattering angle is the angular difference between the incident and scattered waves. (a) Scattering field magnitude (normalized) as a function of angle, and (b) scattering field phase as function of angle.

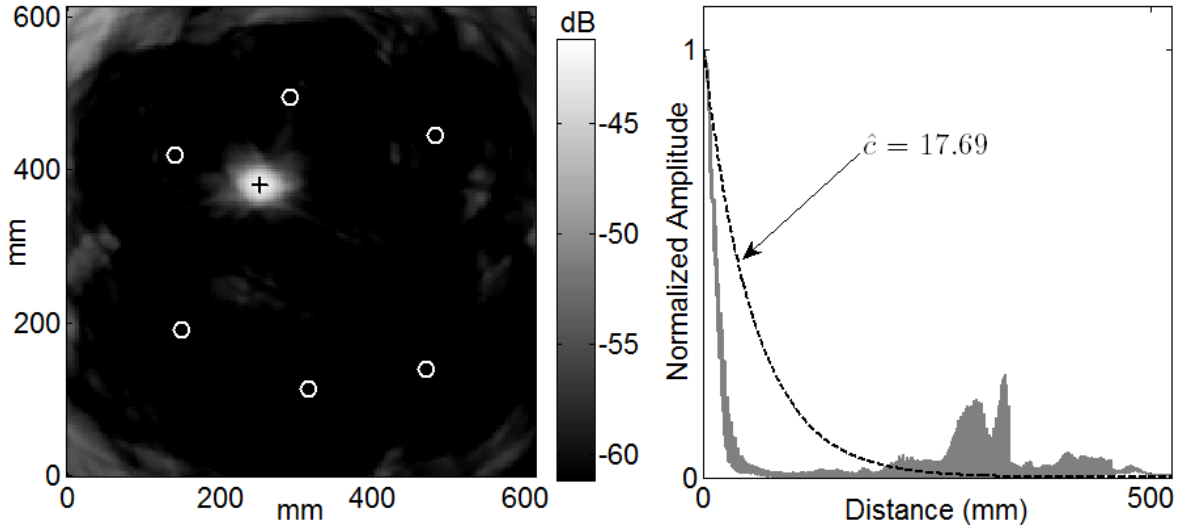


FIGURE 7. MVDR imaging with matched scattering field using simulated envelope signals. (a) Image displayed using a 20 dB scale, and (b) normalized pixel values versus distance from damage location ($\hat{c}$ = 17.69).

approximation derived by Grahn [29] for the center frequency of the propagating signals.

In previous images, the scattering field was assumed to be uniformly distributed (refer to Eq. (8)); however, the simulation actually used scattering characteristics corresponding to a 6 mm through-hole. Figure 6 shows scattered amplitude and phase calculated for a 250 kHz sinusoid incident on a 2 mm through-hole, a 6 mm through-hole, and a uniform scatterer. Note that although the scattering pattern for a through-hole is independent of incident angle, this is not the case for an arbitrary scatterer such as a crack or notch. The concept of a scattering matrix was introduced in [38] to describe far-field scattering from flaws of arbitrary shape.

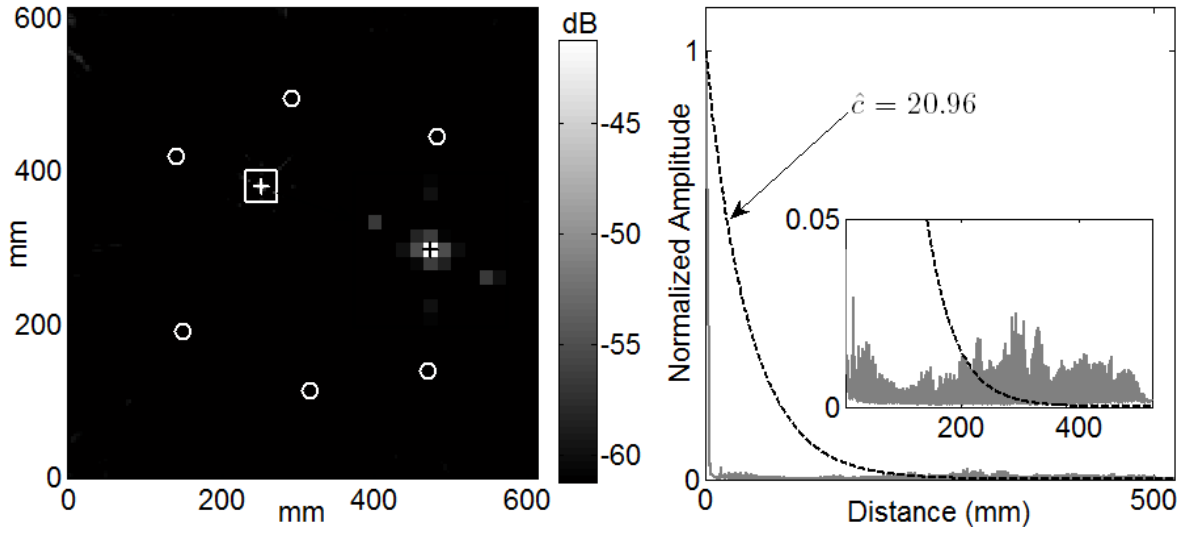


FIGURE 8. MVDR imaging with matched scattering field using simulated analytic signals. (a) Image displayed using a 20 dB scale, and (b) normalized pixel values versus distance from damage location ($\hat{c}$ = 20.96).

Figure 7 shows the performance improvement obtained by incorporating the appropriate scattering field into the look direction. Note that, unlike the other methods discussed in this section, the use of scattering characteristics improves the peak-to-noise ratio of the image by increasing the peak value with little impact on the noise floor. Figure 7 results in a performance metric of $\hat{c}$ = 17.7.

### *D. Phase Information*

Another factor that can significantly improve imaging performance is the inclusion of phase information. Imaging with envelope data, as shown in Figures 3, 4, and 7, discards valuable information contained in the received signals. Two signal formats are available to convey the phase information of the scattered field for imaging: (1) raw RF and (2) analytic representation. Since both formats contain identical information, imaging performance is expected to be comparable between the two. Since the analytic representation treats the signals as complex values, making phase information about the scattered field easily accessible, the analytic representation is used in this paper when phase information is incorporated.

Note that the use of phase information in either format may slightly change two aspects of the imaging algorithm as it has been described: (1) dispersion compensation may become necessary, depending on propagation distances and the degree of dispersion present in the frequency range of operation, and (2) scattering fields will need to include complex reflection coefficients, conveying phase information in addition to magnitude, as in Fig. 6.

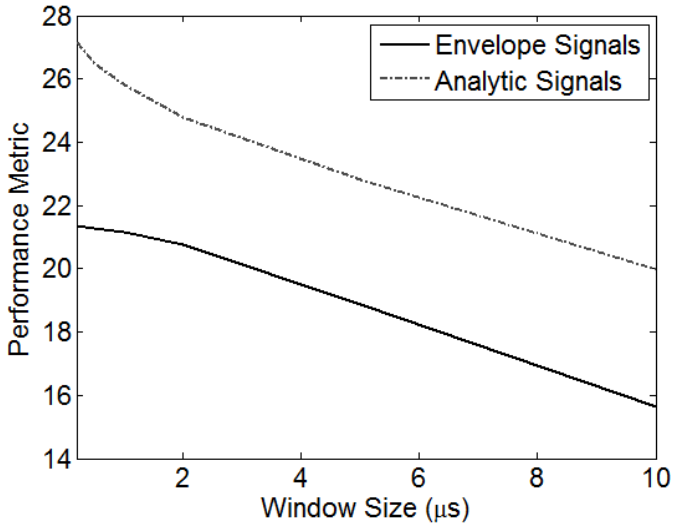


FIGURE 9. MVDR imaging performance as a function of window size using simulated data.

Figure 8 represents the imaging improvements obtained by using phase information, which are manifested by a much smaller defect "spot size" and a significantly lower noise floor. Clearly, the additional phase information provides for significant performance

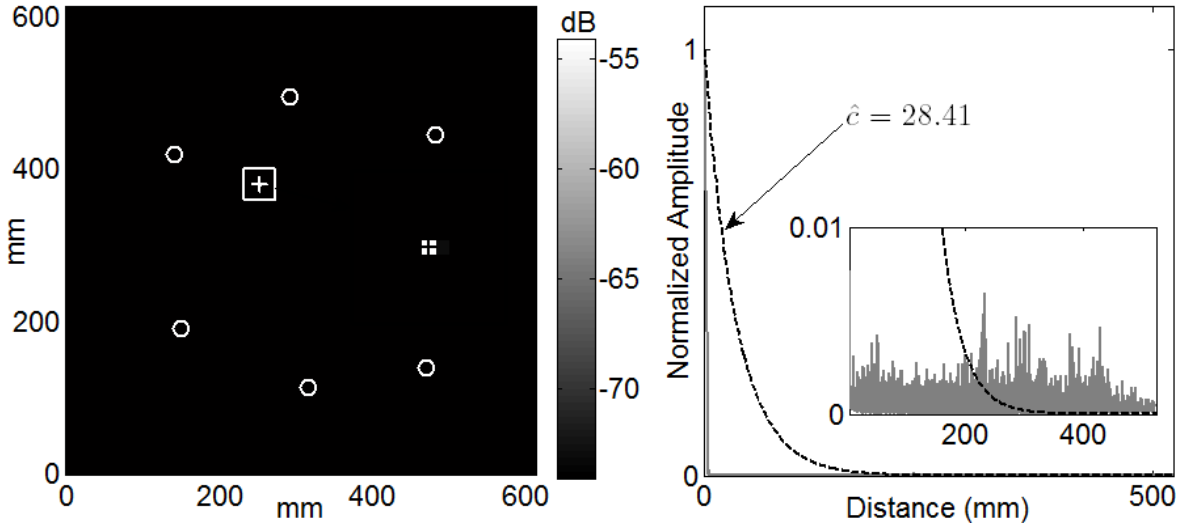


FIGURE 10. MVDR imaging with matched scattering field using simulated analytic signals and a reduced window size. (a) Image displayed using a 20 dB scale, and (b) normalized pixel values versus distance from damage location ( $\hat{c}$ = 28.41).

improvement as compared to the use of envelope signals. The performance metric for Fig. 8 is $\hat{c}$ = 21.0.

There are two fundamental reasons for the significant improvement. First, the use of phase information improves the time resolution of the signal. As the time resolution of the signal is reduced, the spatial resolution of the image is expected to improve. Second, the use of the complex signals for MVDR imaging reduces the image noise floor by reducing the likelihood that the look direction will accidentally agree with $\bar{\mathbf{v}}_1$.

*E. Window Size*

Imaging performance can be further improved by modifying the window width used for the correlation integration in Eq. (7). It is assumed that the same time window is used for all pixel locations, and that it is centered at a time that maximizes the signal-to-noise ratio. For example, for the case illustrated in Fig. 2, the 12 μs integration window is centered at 13 μs.

The length of the time window is determined to balance the need to (1) accurately estimate the correlation matrix and (2) minimize the impact of undesired reflections. For received signals that contain Gaussian white noise, larger time windows provide a mechanism to minimize the effects of noise on the correlation matrix. In contrast, at image locations with artifacts, the pixel value is non-zero because there are non-negligible components of the back-propagated signals that are in agreement with the look direction. Since, non-real-time guided wave systems can reduce the level of additive Gaussian white noise to arbitrary levels by averaging a number of waveforms, increasing the window size simply increases the window of opportunity for undesired agreement between the look direction and non-damage related signals. Therefore, improved performance can be achieved by minimizing the window length.

For the case of high-SNR received signals, the correlation matrix may be accurately generated with as little as a single vector that corresponds to a time that maximizes the signal-to-noise ratio. Figure 9 depicts imaging performance as a function of window size for the simulated case, which uses a Hanning-windowed sinusoid. For more complex excitation signals, it is possible that larger windows may exhibit improved performance.

Note that as the window size is decreased, the correlation matrix used by MVDR becomes underdetermined. As shown previously, however, regularization by diagonal loading is used to mitigate this situation.

Figure 10 illustrates the imaging performance for the test-case after reducing the window-size from the 12 μs window used previously to 0.2 μs. The performance metric is increased from 21.0 to 28.4.

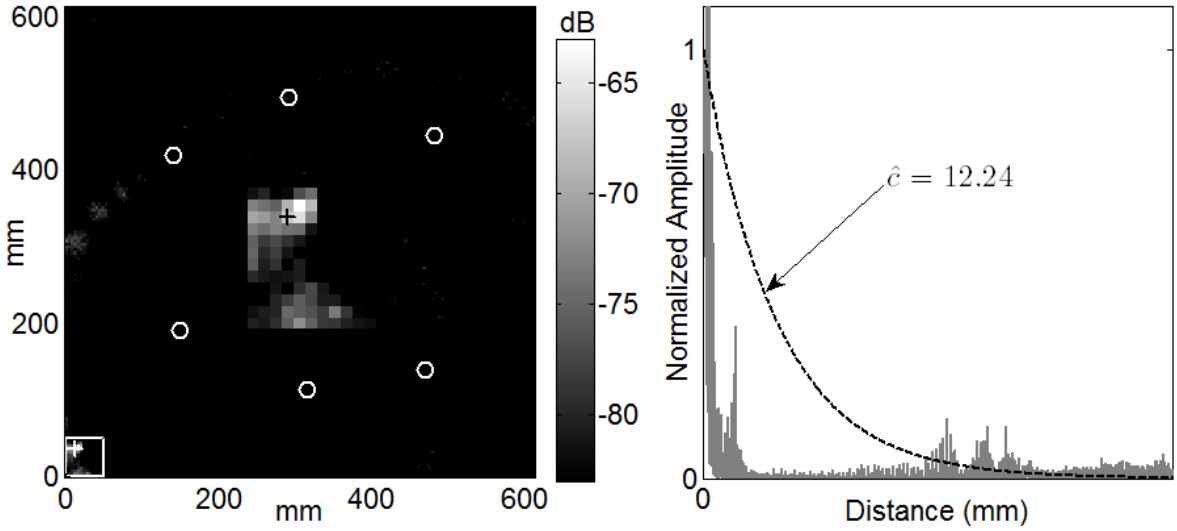


FIGURE 11. MVDR imaging with matched scattering field using simulated analytic signals and a reduced window size. (a) Image of a corner scatterer displayed using a 20 dB scale, and (b) normalized pixel values versus distance from damage location ( $\hat{c}$ = 12.24).

## V. Discussion

In addition to accurate defect localization, minimized artifacts and improved resolution, there are three factors that are of interest in SHM and NDE images: graceful degradation, sensitivity to the damage location, and the ability to perform defect sizing and characterization.

The improved imaging performance demonstrated in Section IV is largely due to the heightened sensitivity resulting from the use of MVDR and phase information. One concern with increased sensitivity is the risk of algorithmic failure in the presence of noise or modeling errors. Modeling errors can include uncompensated or inaccurate receiver phase, scattering information, and dispersion compensation. Figure 5 demonstrates that as $\vec{\mathbf{v}}_1$ and the look direction diverge, the pixel value decays gracefully as a function of the regularization. Therefore, MVDR imaging with phase information is expected to exhibit graceful degradation in the presence of noise or modeling errors if appropriately regularized.

The pixel value obtained using both MVDR imaging and traditional delay-and-sum imaging was shown in Section IV to be equal to the largest eigenvalue of the correlation matrix when the look direction, $\vec{\mathbf{e}}$, is identical to $\vec{\mathbf{v}}_1$. The fact that there is a relationship between the pixel value and largest eigenvalue implies that imaging performance is sensitive to location. When damage is close to the sensors, the propagation distances are short and received signals are strong, resulting in a large $\lambda_1$, but when damage is far from the sensors, the received signals are weaker, resulting in a smaller $\lambda_1$. Intuitively, normalizing the covariance matrices to have unit norm would correct for this, making the imaging algorithm less sensitive to pixel location. Alternatively, the received signals can be adjusted in amplitude as a function of time or distance to compensate for geometric spreading. In actuality, however, normalization of covariance matrices and time or distance amplitude compensation introduces artifacts because they effectively amplify pixel values that originally had no, or very little, signal present. Without normalization, pixels located further away from the array (in particular, outside the bounding polygon) do have smaller amplitudes. However, the reduced amplitude has far less of an adverse impact than the artifacts introduced by covariance normalization or signal amplitude compensation. In simulations, imaging of damage in the corners of the plate still produces impressive results, as shown in Fig. 11.

Finally, defect characterization, including sizing, is a major goal of imaging with SHM and NDE systems. It is desirable for the image to reflect the relative magnitudes of the defects, meaning that a larger damage site should have a larger pixel value. For the simple case of multiple uniform scatterers of varying sizes, MVDR imaging can produce such relative pixel values if

compensation is made for geometric propagation loss. As mentioned in the previous paragraph, however, this comes at the expense of introducing artifacts by amplifying noise in the received signals. In realistic environments, damage sites of different sizes will have different scattering fields. As such, the sensitivity to scattering fields provides an alternative mechanism to characterize both the size and type of damage, which is the subject of ongoing research efforts.

## VI. Experimental Results

The proposed techniques to reduce imaging artifacts were applied to previously collected experimental data originally reported in [24]. The experimental setup is similar to the simulated test-case discussed throughout the paper. Six PZT transducers were arranged as in Fig. 1 on a 610 x 610 x 4.76 mm aluminum 6061 plate. A impulsive excitation was used to excite the transmitters, and broadband received signals were sampled at 25 MHz. A total of 15 different transmitter-receiver pairs were used. After baseline data were collected, a 2 mm diameter through-hole was drilled at the location indicated in Fig. 1. Expected scattering characteristics for imaging were generated using the technique proposed by Grahn [29] for incident and scattered $S_0$ waves at 250 kHz, which is the dominant mode here. Dispersion compensation was not performed.

Figures 12 and 13 illustrate imaging performance using traditional delay-and-sum imaging as described in Section III. Figure 12 was generated using the envelope of the analytic signal, while Fig. 13 was generated with the analytic signal itself. Note that even with delay-and-sum imaging, the use of phase information improves the imaging performance, although the resulting image of Fig. 13(b) has a relatively high noise floor.

Figures 14 and 15 illustrate imaging performance using MVDR as described in Section IV. As in Figures 12 and 13, Fig. 14 was generated using the envelope of the analytic signal, while Fig. 15 used the analytic signal. Note that the increased noise floor observed in Fig. 15, as compared to the simulated equivalent of Fig. 10, is most likely due to the combination of imperfect baseline subtraction, lack of dispersion compensation, and errors in the approximated scattering characteristics. These inaccuracies result in the peak not reaching the maximum possible value, which is manifested in both plots of Fig. 15 as an increased noise floor.

## VII. Conclusion

This paper has identified four techniques for reducing artifacts typically observed in guided wave imaging. The use of MVDR for imaging was motivated mathematically and demonstrated with both simulated and experimental signals. After introducing the concept of MVDR imaging, images were further improved by incorporating scattering field information into the look direction. The inherent ability of the MVDR algorithm to suppress imaging artifacts was then shown to further enhance images when the analytic representation of the received signals is used, which includes phase information. Finally, for high SNR environments, a direct relationship was shown between the time integration window length and the presence and amplitude of imaging artifacts. Improvement was demonstrated quantitatively for each technique using a custom performance metric.

The primary contributions of the paper include the application of the MVDR algorithm to *in situ* guided wave imaging applications with spatially distributed arrays, a quantification of the improvements achieved when phase and scattering information are used in conjunction with MVDR, and an identification of the importance of minimizing the window size when operating in a high SNR environment. For *in situ* guided wave imaging systems with spatially distributed arrays, which must balance system complexity and cost with imaging performance, the improved ability to detect and localize damage demonstrated here has clear significance. The methods illustrated here could also be readily applied to conventional compact bulk and guided wave arrays operating in the near field. Future work remains in defect sizing and characterization, accommodating frequency-dependent scattering fields, and improving experimental performance through more accurate system phase characterization.

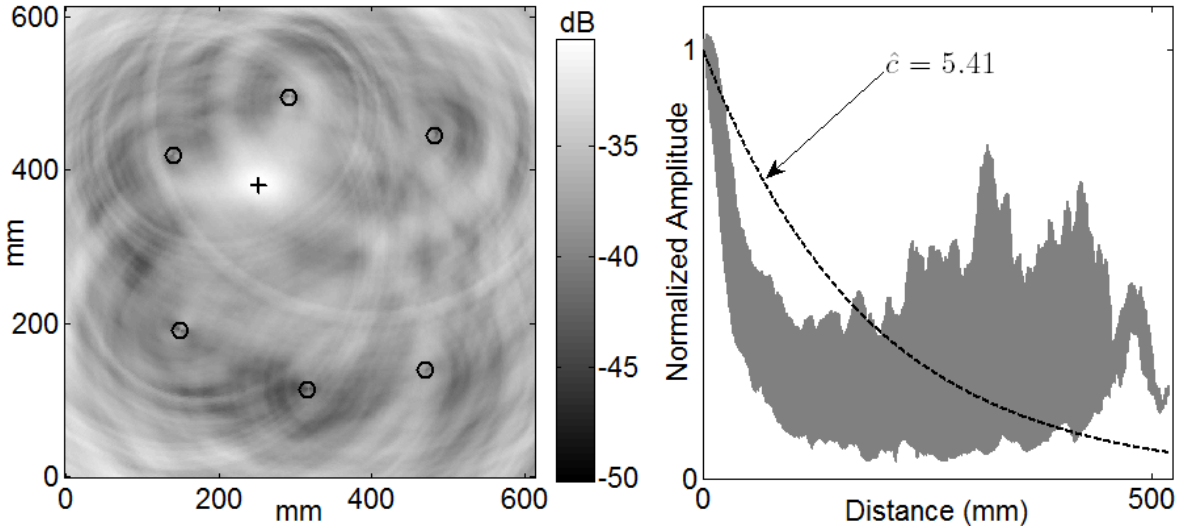


FIGURE 12. Delay-and-sum imaging with experimental data of a 2 mm through-hole. Imaging was performed with envelope signals, a 0.2 μs window, and the 2 mm scattering field generated as per Grahn [37]. (a) Image displayed using a 20 dB scale, and (b) normalized pixel values versus distance from damage location ( $\hat{c}$ = 5.41).

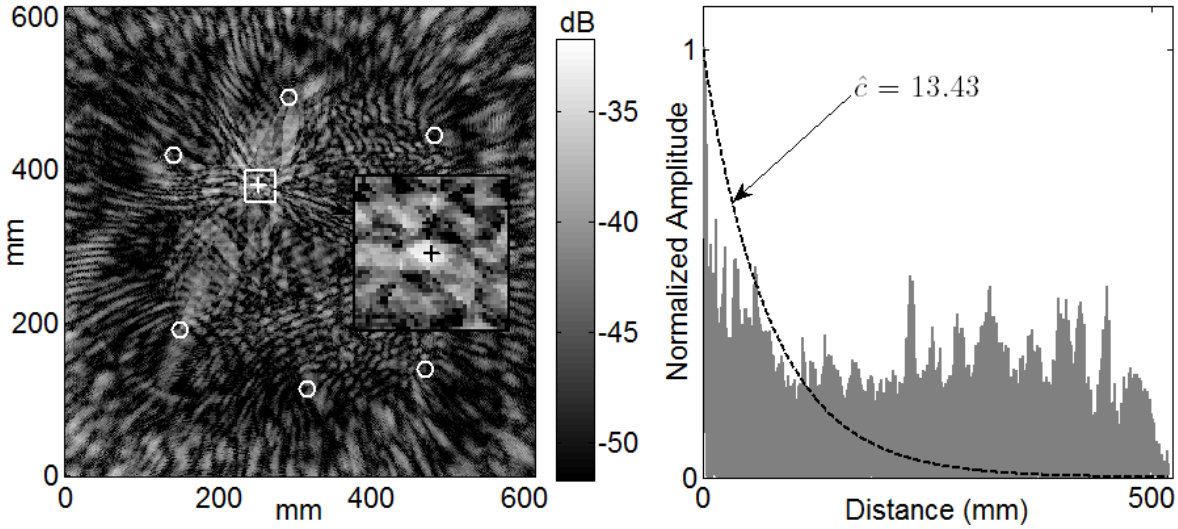


FIGURE 13. Delay-and-sum imaging with experimental data from a 2 mm through-hole. Imaging was performed with complex (analytic) signals, a 0.2 μs window, and the 2 mm scattering field generated as per Grahn [37]. (a) Image displayed using a 20 dB scale, and (b) normalized pixel values versus distance from damage location ( $\hat{c}$ = 13.43).

## REFERENCES

[1] J. L. Rose, "A baseline and vision of ultrasonic guided wave inspection potential," *J. Pressure Vessel Technol.*, vol. 124, pp. 273-282, 2002.

[2] J. E. Michaels, J. S. Hall, G. Hickman *et al.*, "Sparse array imaging of change-detected signals by minimum variance processing," *Rev. Prog. Quant. Ultrason. Nondestr. Eval.*, vol. 28, pp. 642-649, 2009.

[3] J. E. Michaels, J. S. Hall, and T. E. Michaels, "Adaptive imaging of damage from changes in guided wave signals recorded from spatially distributed arrays," *Proc. SPIE*, vol. 7295, pp. 72915:1-11, 2009.

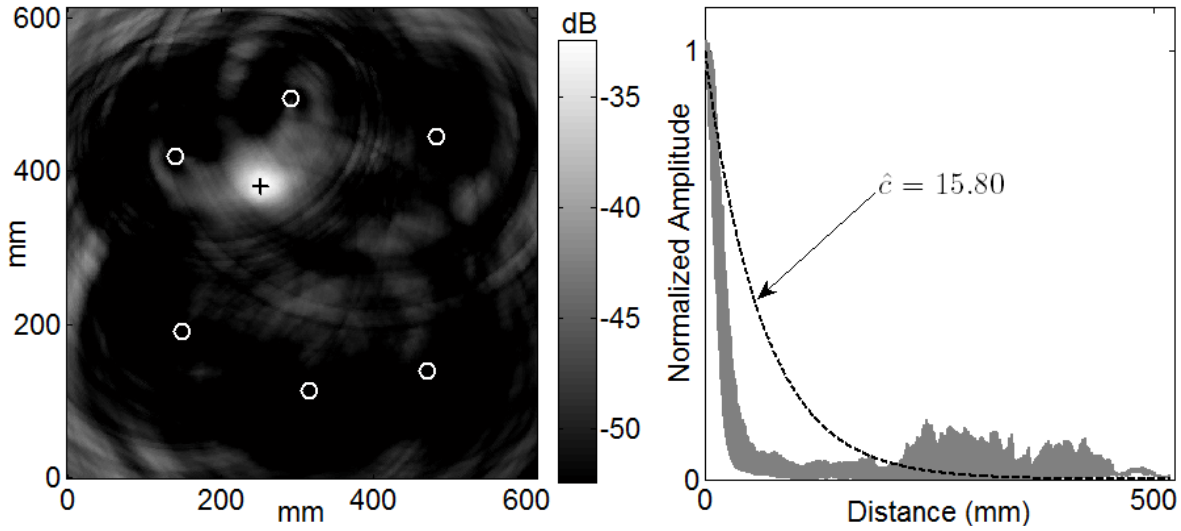


FIGURE 14. MVDR imaging with experimental data from a 2 mm through-hole. Imaging was performed with envelope signals, a 0.2 μs window, and the 2 mm scattering field generated as per Grahn [37]. (a) Image displayed using a 20 dB scale, and (b) normalized pixel values versus distance from damage location ( $\hat{c}$ = 15.80).

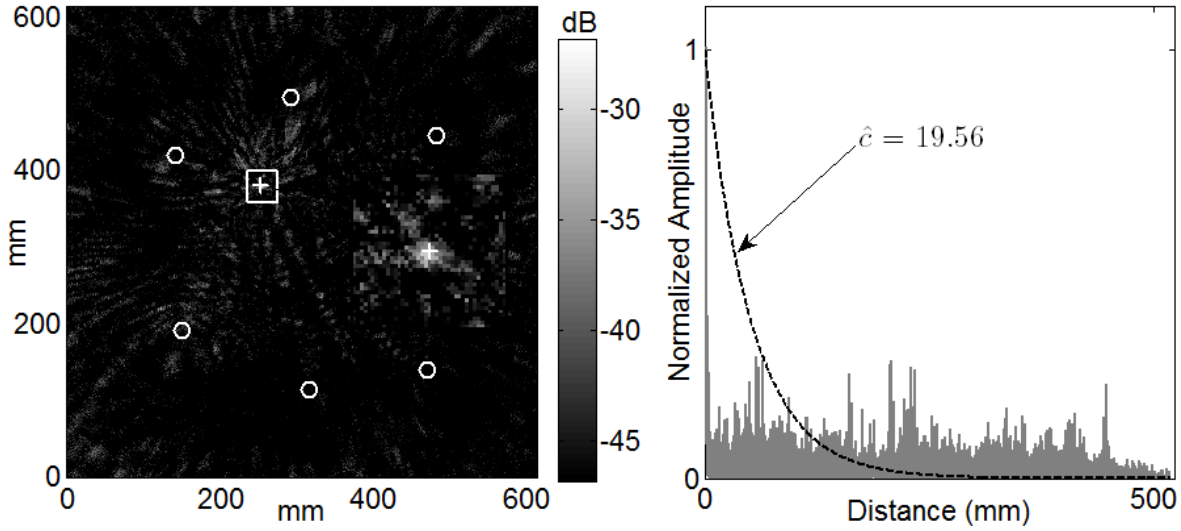


FIGURE 15. MVDR imaging with experimental data from a 2 mm through-hole. Imaging was performed with complex (analytic) signals, a 0.2 μs window, and the 2 mm scattering field generated as per Grahn [37]. (a) Image displayed using a 20 dB scale, and (b) normalized pixel values versus distance from damage location ( $\hat{c}$ = 19.56).

[4] O. L. Frost, III, "An algorithm for linearly constrained adaptive array processing," *Proc. IEEE*, vol. 60, no. 8, pp. 926-935, 1972.

[5] J. Capon, "High-resolution frequency-wavenumber spectrum analysis," *Proc. IEEE*, vol. 57, no. 8, pp. 1408-1418, 1969.

[6] A. Velichko, and P. D. Wilcox, "Guided wave arrays for high resolution inspection," *J. Acoust. Soc. Am.*, vol. 123, no. 1, pp. 186-196, 2008.

[7] P. D. Wilcox, A. J. Croxford, and B. W. Drinkwater, "Sensitivity limitations for guided wave structural health monitoring," *Proc. SPIE*, vol. 6532, pp. 65320A:1-9, 2007.

[8] P. D. Wilcox, G. Konstantinidis, and B. W. Drinkwater, "Structural health monitoring using sparse distributed networks of guided wave sensors," *Proc. SPIE*, pp. 61731L:1-12, 2006.

[9] Y. Lu, and J. E. Michaels, "A methodology for structural health monitoring with diffuse ultrasonic waves in the presence of temperature variations," *Ultrasonics*, vol. 43, pp. 717-731, 2005.

[10] G. Konstantinidis, B. W. Drinkwater, and P. D. Wilcox, "The temperature stability of guided wave structural health monitoring systems," *Smart Mater. Struct.*, vol. 15, pp. 967-976, 2006.

[11] T. Clarke, F. Simonetti, and P. Cawley, "Guided wave health monitoring of complex structures by sparse array systems: Influence of temperature changes on performance," *J. Sound and Vib.*, 2009.

[12] A. J. Croxford, P. D. Wilcox, Y. Lu *et al.*, "Quantification of environmental compensation strategies for guided wave structural health monitoring," *Proc. SPIE*, vol. 6935, pp. 69350H:1-11, 2008.

[13] A. J. Croxford, P. D. Wilcox, C. R. P. Courtney *et al.*, "SHM in complex structural components," *Proc. SPIE*, vol. 7295, pp. 792503:1-12, 2009.

[14] D. P. Jansen, and D. A. Hutchins, "Lamb wave tomography," *IEEE Ultrason. Symp. Proc.*, vol. 2, pp. 1017-1020, 1990.

[15] T. R. Hay, R. L. Royer, H. Gao *et al.*, "A comparison of embedded sensor Lamb wave ultrasonic tomography approaches for material loss detection," *Smart Mater. Struct.*, vol. 15, pp. 946-951, 2006.

[16] H. Gao, Y. Shi, and J. L. Rose, "Guided wave tomography on an aircraft wing with leave in place sensors," *Rev. Prog. Quant. Ultrason. Nondestr. Eval.*, vol. 24, pp. 1788-1794, 2005.

[17] C. H. Wang, J. T. Rose, and F.-K. Chang, "A synthetic time-reversal imaging method for structural health monitoring," *Smart Mater. Struct.*, vol. 13, pp. 415-423, 2004.

[18] J. E. Michaels, and T. E. Michaels, "Enhanced differential methods for guided wave phased array imaging using spatially distributed piezoelectric transducers," *Rev. Prog. Quant. Ultrason. Nondestr. Eval.*, vol. 25, pp. 837-844, 2006.

[19] J. E. Michaels, A. J. Croxford, and P. D. Wilcox, "Imaging algorithms for locating damage via in situ ultrasonic sensors," *Proc. 2008 IEEE Sens. Appl. Symp.*, pp. 63-67, 2008.

[20] J. E. Michaels, and T. E. Michaels, "Guided wave signal processing and image fusion for in situ damage localization in plates," *Wave Motion*, vol. 44, pp. 482-492, 2007.

[21] A. J. Croxford, P. D. Wilcox, and B. W. Drinkwater, "Guided wave SHM with a distributed sensor network," *Proc. SPIE*, vol. 6935, pp. 693514:1-9, 2008.

[22] J. L. Rose, *Waves in Solid Media*, Cambridge, UK: Cambridge University Press, 1999.

[23] P. D. Wilcox, M. J. S. Lowe, and P. Cawley, "The effect of dispersion on long-range inspection using ultrasonic guided waves," *NDT and E Int.*, vol. 34, no. 1, pp. 1-9, 2001.

[24] J. E. Michaels, "Detection, localization and characterization of damage in plates with an in situ array of spatially distributed sensors," *Smart Mater. Struct.*, vol. 17, no. 035035, pp. 1-15, 2008.

[25] A. J. Croxford, P. D. Wilcox, B. W. Drinkwater *et al.*, "Strategies for guided-wave structural health monitoring," *Proc. R. Soc. A*, vol. 463, pp. 2961-2981, 2007.

[26] R. Sicard, J. Goyette, and D. Zellouf, "A numerical dispersion compensation technique for time recompression of Lamb wave signals," *Ultrasonics*, vol. 40, pp. 727-732, 2002.

[27] P. D. Wilcox, "Omni-directional guided wave transducer arrays for the rapid inspection of large areas of plate structures," *IEEE Trans. Ultrason., Ferroelectr., Freq. Control*, vol. 50, no. 6, pp. 699-709, 2003.

[28] P. D. Wilcox, "A rapid signal processing technique to remove the effect of dispersion from guided wave signals," *IEEE Trans. Ultrason., Ferroelectr., Freq. Control*, vol. 50, no. 4, pp. 419-427, 2003.

[29] T. Grahn, "Lamb wave scattering from a circular partly through-thickness hole in a plate," *Wave Motion*, vol. 37, pp. 63-80, 2003.

[30] D. Johnson, and D. Dudgeon, *Array Signal Processing Concepts and Techniques*, Upper Saddle River, NJ: Prentice Hall, 1993.

[31] B. D. Carlson, "Covariance matrix estimation errors and diagonal loading in adaptive arrays," *IEEE Trans. Aerosp. Electron. Sys.*, vol. 24, no. 4, pp. 397-401, 1988.

[32] H. Cox, R. M. Zeskind, and M. M. Owen, "Robust adaptive beamforming," *IEEE Trans. Acoust. Speech Signal Process.*, vol. ASSP-35, no. 10, pp. 1365-1376, 1987.

[33] Y. Cho, D. D. Hongerholt, and J. L. Rose, "Lamb wave scattering analysis for reflector characterization," *IEEE Trans. Ultrason., Ferroelectr., Freq. Control*, vol. 44, no. 1, pp. 44-52, 1997.

[34] J. C. P. McKeon, and M. K. Hinders, "Lamb wave scattering from a through hole," *J. Sound and Vib.*, vol. 224, no. 5, pp. 843-862, 1999.

[35] O. Diligent, T. Grahn, A. Boström *et al.*, "The low-frequency reflection and scattering of the S0 Lamb mode from a circular through-thickness hole in a plate: Finite Element, analytical and experimental studies," *J. Acoust. Soc. Am.*, vol. 111, no. 1, pp. 64-74, 2002.

[36] Z. Chang, and A. Mal, "Scattering of Lamb waves from a rivet hole with edge cracks," *Mech. Mater.*, vol. 31, pp. 197-204, 1999.

[37] M. J. S. Lowe, and O. Diligent, “Low-frequency reflection characteristics of the S0 Lamb wave from a rectangular notch in a plate,” *J. Acoust. Soc. Am.*, vol. 111, no. 1, pp. 64-74, 2002.

[38] J. Zhang, B. W. Drinkwater, and P. D. Wilcox, “Defect characterization using an ultrasonic array to measure the scattering coefficient matrix,” *IEEE Trans. Ultrason., Ferroelectr., Freq. Control*, vol. 55, no. 10, pp. 2254-2265, 2008.